Growth model of binary alloy nanopowders for thermal plasma synthesis

doi: 10.1063/1.3464228

Growth model of binary alloy nanopowders for thermal plasma synthesis

Masaya Shigeta[1,a)] and Takayuki Watanabe[2,b)]
[1]*Department of Mechanical Systems and Design, Graduate School of Engineering, Tohoku University, 6-6-01 Aramaki-Aoba, Aoba-ku, Sendai 980-8579, Japan*
[2]*Department of Environmental Chemistry and Engineering, Interdisciplinary Graduate School of Science and Engineering, Tokyo Institute of Technology, 4259-G1-22 Nagatsuta, Midori-ku, Yokohama 226-8503, Japan*

(Received 19 April 2010; accepted 15 June 2010; published online 23 August 2010)

A new model is developed for numerical analysis of the entire growth process of binary alloy nanopowders in thermal plasma synthesis. The model can express any nanopowder profile in the particle size-composition distribution (PSCD). Moreover, its numerical solution algorithm is arithmetic and straightforward so that the model is easy to use. By virtue of these features, the model effectively simulates the collective and simultaneous combined process of binary homogeneous nucleation, binary heterogeneous cocondensation, and coagulation among nanoparticles. The effect of the freezing point depression due to nanoscale particle diameters is also considered in the model. In this study, the metal–silicon systems are particularly chosen as representative binary systems involving cocondensation processes. In consequence, the numerical calculation with the present model reveals the growth mechanisms of the Mo–Si and Ti–Si nanopowders by exhibiting their PSCD evolutions. The difference of the materials' saturation pressures strongly affects the growth behaviors and mature states of the binary alloy nanopowder. © *2010 American Institute of Physics*. [doi:10.1063/1.3464228]

I. INTRODUCTION

Nanopowder has attracted interests of numerous and varied engineering researchers because it exhibits unique capabilities that differ greatly from those of bulk materials or powders composed of larger particles.[1] In particular, the nanopowders composed of binary alloy nanoparticles are anticipated as potentially useful materials.[2] For instance, nanoparticles of metal–silicides (e.g., $MoSi_2$ and $TiSi_2$) have been synthesized for extremely small electronic and mechanical applications such as solar-controlled windows, electromagnetic shielding, and contact materials in microelectronics. However, because the raw materials usually have high melting points or boiling points, high-rate synthesis of binary alloy nanopowders is almost impossible using conventional methods such as liquid-phase deposition or grinding techniques. Even combustion processes are ineffectual because the combustion flame cannot reach sufficiently high temperatures to vaporize the raw materials; furthermore, the oxidation atmosphere for combustion causes unfavorable production of contaminants.

To surmount those obstacles, thermal plasmas have been used for the effective synthesis of binary alloy nanopowders[3–9] because thermal plasmas offer several following distinctive advantages: high enthalpy, high chemical reactivity, variable properties, and steep temperature gradients. Additionally, thermofluid fields such as temperature and velocity are controllable using external electromagnetic fields.[10–12]

Thermal plasma synthesis of binary alloy nanopowders starts from vaporization of the raw materials in the high-enthalpy field of the plasma. The binary metal vapors are transported with the flow to the plasma tail where the temperature drastically decreases. Consequently, the metal vapors become supersaturated, which engenders homogeneous nuclei composed of two materials (binary nucleation). Immediately, the binary metal vapors cocondense heterogeneously on the nuclei (binary condensation). Additionally, during their growth, the nanoparticles mutually collide and merge into larger nanoparticles (coagulation). These three processes progress collectively and simultaneously in a few tens of milliseconds; furthermore, the materials often have a large difference of their saturation pressures. In consequence, the growth of binary alloy nanopowders is tremendously complicated and such nanopowders have varieties of sizes and compositions. Therefore, in addition to the high demand in industry, although the morphology of binary alloy nanopowders is of great interest from the scientific viewpoint of physics and chemistry as well as engineering, the detailed mechanism of their collective growth remains poorly understood. This is true because it is impossible to observe every process using experimental approaches directly; only the characteristics of the final products can be evaluated.

On the other hand, theoretical and numerical studies have also been carried out to clarify the binary growths and to predict the profiles of nanopowders that will be synthesized. Lümmen and Kraska applied molecular dynamics (MDs) simulation to a binary alloy system.[13] However, they were only able to simulate the several-nanosecond formation of a few tens of nuclei which are the embryos of nanoparticles. MD simulation cannot treat the whole growth process from nucleation until nanopowders complete their growth because of computational resource limitations.

Meanwhile, in place of such a scheme, which requires a

a)Electronic mail: shigeta@fluid.mech.tohoku.ac.jp.
b)Electronic mail: watanabe@chemenv.titech.ac.jp.

heavy computational load, a few models based on aerosol dynamics have been used to simulate the whole process of nanopowders' collective growth involving cocondensations of binary metal vapors.[9,14–17] However, those models had to adopt several oversimplifications to obtain even simple numerical solutions; moreover, the solutions were only mean values. We therefore developed a unique solution algorithm—*two-directional nodal model*—to analyze nanopowders' growth numerically in binary systems.[18] That easy-to-use model can express any profile of particle size-composition distribution (PSCD) of a nanopowder. In addition, the numerical solution algorithm itself was arithmetic and straightforward. However, in that model, the nucleation and condensation were described simply using theories for a unary system even though binary systems were analyzed. This simplification led to an error that the nucleation produced nuclei with only a single component. In fact, the nuclei can contain two components. Also, an undersaturated vapor can condense heterogeneously on nanoparticles of binary mixtures, which was not expressed in our previous model.

In this study, by combining our solution algorithm with the theory for binary homogeneous nucleation and the theory for binary heterogeneous condensation, a new model is developed that can effectively simulate the whole growth process of binary alloy nanopowders for thermal plasma synthesis. Additionally, the freezing point depression of nanoparticles due to their small sizes is taken into account to determine the final state of nanopowders.

To verify the present model, numerical calculations of the metal–silicide nanopowders' growths are demonstrated for comparison with the available experiment results, because only the literatures of the metal–silicide nanopowder synthesis[8,9] describe the specific data of the plasma generating conditions as well as the nanopowders' profiles. In consequence, the growth behaviors of those binary alloy nanopowders are also clarified.

II. MODEL DESCRIPTION

A. Concepts and assumptions

The present model is developed based on the following concepts: (A) it is easy to use from an engineering viewpoint; (B) it can express any profile of a nanopowder in a PSCD; (C) its numerical solution algorithm is arithmetic and straightforward.

For model formulation, the following assumptions are introduced: (i) nanoparticles composing nanopowders are spherical; (ii) the nanoparticle's inertia is negligible; (iii) the temperature of nanopowder is identical to that of the bulk gas surrounding them; (iv) heat generated by condensation is negligible; (v) the electric charge of nanopowder is also negligible; and (vi) the material vapors are regarded as an ideal gas.

Nanopowder growth involves three fundamental processes requiring different time resolutions: 10^{-15} s for homogeneous nucleation,[13] 10^{-5} s for heterogeneous condensation, and 10^{-4} s for coagulation among nanoparticles. If numerical calculation were conducted with the time resolution for homogeneous nucleation, an enormous computational load and long run-time would be necessary to simulate the whole process of a nanopowder's growth, which is impractical. Consequently, in this study, numerical calculation is conducted with the time resolution for heterogeneous condensation. Although the transient process in nucleation is not considered, the theory[19] gives the accurate values of size, composition, and birth rate of stable nuclei; and those values are all that the present model requires for its nucleation regime. This manner makes it feasible to simulate the whole growth process.

B. Solution algorithm on two-directional nodal discretization

The present model incorporates not only a single nanoparticle's growth but also nanoparticles' collective growth. Such nanopowder growth is described well by the general dynamic equation (GDE) for aerosol.[20] However, the GDE is usually very arduous to solve even for a unary nanopowder, not to mention a binary alloy nanopowder. Therefore, to solve the GDE for a binary system effectively, our previous work[18] introduced the PSCD in place of the often-used particle size distribution (PSD). The PSCD is described by nodal discretization for the two individual directions of the particle size and composition, where nanoparticles composing a nanopowder reside only at the nodes.

The nodes are spaced linearly on a logarithmic scale along the size axis to cover the wide range of particle sizes:

$$v_{k+1} = f_v v_k \quad (k = 1,2, \ldots, k_{max} - 1). \tag{1}$$

Therein, v is the particle volume and subscript k represents the node number along the size axis. The geometric spacing factor for size f_v and number of nodes k_{max} are chosen, respectively, as 1.6 and 54. These values provide sufficient accuracy for the size range of a nanopowder synthesized in thermal plasma processing (see Appendix A). The particle volume at the first node is arbitrarily set to a 10-mer of material M:

$$v_1 = 10 v_{mono(M)}. \tag{2}$$

In that equation, $v_{mono(M)}$ is the volume of the monomer of material M.

The nodes are linearly spaced along the composition axis:

$$x_{n+1} = x_n + \Delta x \quad (n = 1,2, \ldots, n_{max} - 1). \tag{3}$$

In that equation, x is the mole fraction of material B in a particle and subscript n denotes the node number along the composition axis. The increment Δx is chosen as 0.025; the number of nodes n_{max} is 41. The particles at the first node contain only material A, whereas the composition of the particles at the n_{max}th node is 100% material B:

$$x_1 = 0, \tag{4}$$

and

$$x_{n_{max}} = 1. \tag{5}$$

In the size-composition space, the particle concentration N at node (k,n) is written as

$$\frac{dN_{k,n}}{dt} = [\dot{N}_{k,n}]_{nucl} + [\dot{N}_{k,n}]_{cond} + [\dot{N}_{k,n}]_{coag}, \tag{6}$$

where t is the time and $[\dot{N}]$ represents the net production rate. The subscripts *nucl*, *cond*, and *coag* stand for the contributions from binary nucleation, binary condensation, and coagulation of particles.

The net production rate attributable to the binary homogeneous nucleation is given as

$$[\dot{N}_{k,n}]_{nucl} = I^* \xi_k^{(nucl)} \psi_n^{(nucl)}. \tag{7}$$

Therein, I^* is the homogeneous nucleation rate: the number of nucleus generated per unit volume and unit time. The solution algorithm of the binary nucleation process is presented in Fig. 1(a). A nucleus is in the critical state; its size v^* is determined by the balance between growth and evaporation. Therefore, a nucleus smaller than size v^* easily evaporates and cannot exist as a particle. Consequently, only the next larger nodes can gain the nuclei. Considering the conservation of the particle volume, the splitting operators along the size axis ξ and along the composition axis ψ are given as

$$\xi_k^{(nucl)} = \begin{cases} \dfrac{v^*}{v_k}; & if(v_{k-1} \le v^* < v_k) \\ \dfrac{v^*}{v_2}; & if(v^* < v_1) \\ 0; & \text{otherwise} \end{cases}, \tag{8}$$

and

$$\psi_n^{(nucl)} = \begin{cases} \dfrac{x_{n+1} - x^*}{x_{n+1} - x_n}; & if(x_n \le x^* < x_{n+1}) \\ \dfrac{x^* - x_{n-1}}{x_n - x_{n-1}}; & if(x_{n-1} \le x^* < x_n) \\ 0; & \text{otherwise} \end{cases}. \tag{9}$$

The nucleus' size v^* and composition x^* are determined by both the material properties and the states of the vapors (e.g., the temperature and the supersaturation ratio), as described in Sec. II C 1.

Figure 1(b) presents the solution algorithm of the binary heterogeneous condensation process. All particles at node (i,l) grow to new particles with the volume $v_i + \Delta v_{(A)i,l} + \Delta v_{(B)i,l}$ and the composition $x_{i,l}^{\prime(cond)}$ by gaining vapors during the infinitesimal time increment Δt, where $\Delta v_{(M)i,l}$ is the volume increment of each particle at node (i,l) because of the condensation of material M for Δt. The new particles are

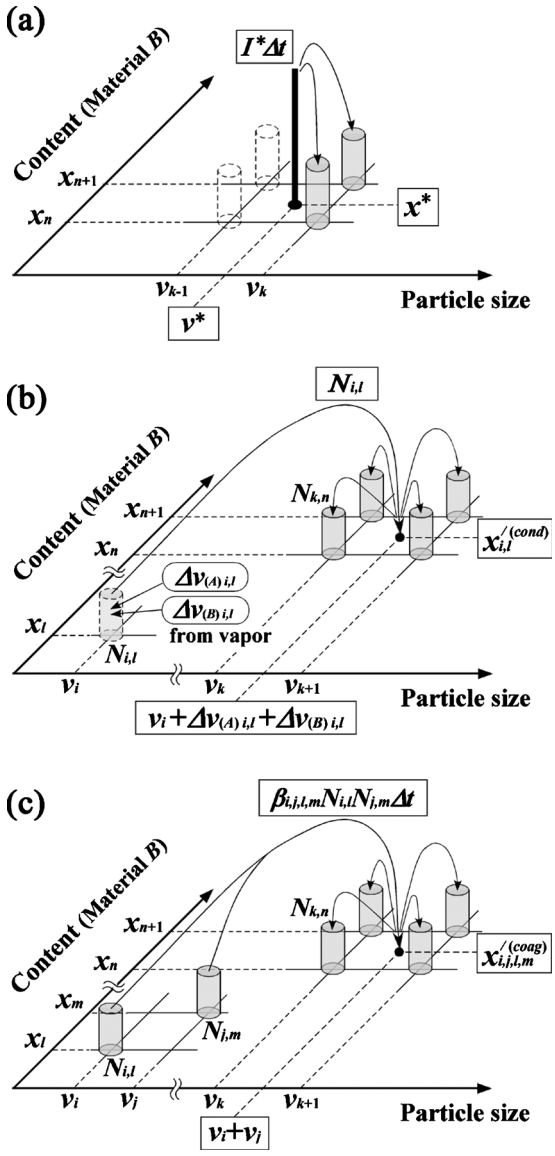

FIG. 1. Solution algorithms: (a) binary homogeneous nucleation, (b) binary heterogeneous condensation, and (c) coagulation between particles with different sizes and compositions.

distributed to the adjacent nodes under the mass-conserving condition. It is noted that node (i,l) becomes empty. Therefore, the net production rate of the binary condensation can be written as

$$[\dot{N}_{k,n}]_{cond} = \sum_i \sum_l \frac{(\xi_{i,l,k}^{(cond)} \psi_{i,l,n}^{(cond)} - \delta_{i,k}\delta_{l,n}) N_{i,l}}{\Delta t}. \tag{10}$$

The splitting operators are given as

$$\xi_{i,l,k}^{(cond)} = \begin{cases} \dfrac{v_{k+1} - (v_i + \Delta v_{(A)i,l} + \Delta v_{(B)i,l})}{v_{k+1} - v_k}; & if(v_k \le v_i + \Delta v_{(A)i,l} + \Delta v_{(B)i,l} < v_{k+1}) \\ \dfrac{(v_i + \Delta v_{(A)i,l} + \Delta v_{(B)i,l}) - v_{k-1}}{v_k - v_{k-1}}; & if(v_{k-1} \le v_i + \Delta v_{(A)i,l} + \Delta v_{(B)i,l} < v_k) \\ 0; & \text{otherwise} \end{cases}, \tag{11}$$

and

$$\psi_{i,l,n}^{(cond)} = \begin{cases} \dfrac{x_{n+1} - x_{i,l}'^{(cond)}}{x_{n+1} - x_n}; & if(x_n \le x_{i,l}'^{(cond)} < x_{n+1}) \\ \dfrac{x_{i,l}'^{(cond)} - x_{n-1}}{x_n - x_{n-1}}; & if(x_{n-1} \le x_{i,l}'^{(cond)} < x_n) \\ 0; & \text{otherwise} \end{cases} . \tag{12}$$

In those equations, $\delta_{i,k}$ represents the Kronecker delta:

$$\delta_{i,k} = \begin{cases} 1; & if(i = k) \\ 0; & if(i \neq k) \end{cases} . \tag{13}$$

Figure 1(c) depicts the solution algorithm of the coagulation process among particles. The net production rate at node (k,n) because of coagulation, is written as shown below.

$$[\dot{N}_{k,n}]_{coag} = \frac{1}{2}\sum_i \sum_j \sum_l \sum_m \xi_{i,j,k}^{(coag)} \psi_{i,j,l,m,n}^{(coag)} \beta_{i,j,l,m} N_{i,l} N_{j,m} - N_{k,n} \sum_i \sum_l \beta_{i,k,l,n} N_{i,l}. \tag{14}$$

That is Smoluchowski's equation modified with splitting operators for coagulation. Subscripts i and j denote the node numbers along the size axis, whereas subscripts l and m signify those along the composition axis. Unlike the algorithms of the binary nucleation and the binary condensation, only this algorithm of the coagulation was built by expanding the framework for a free-molecular unary system.[21] However, this study adopts the different formula of the collision frequency function β which will covers the wider range of particle sizes (see Sec. II C 3). The first term of the right-hand side describes the particle gain at node (k,n) attributable to collisions between the particles at the other nodes. The second term of the right-hand side expresses the particle loss at node (k,n) attributable to collisions between the particles at node (k,n) and the particles at the other nodes. Particles with volumes v_i and v_j collide and coagulate, and consequently form a new particle with the volume v_i+v_j and the composition $x_{i,j,l,m}'^{(coag)}$. Therefore, the splitting operators are written as

$$\xi_{i,j,k}^{(coag)} = \begin{cases} \dfrac{v_{k+1} - (v_i + v_j)}{v_{k+1} - v_k}; & if(v_k \le v_i + v_j < v_{k+1}) \\ \dfrac{(v_i + v_j) - v_{k-1}}{v_k - v_{k-1}}; & if(v_{k-1} \le v_i + v_j < v_k) \\ 0; & \text{otherwise} \end{cases} , \tag{15}$$

and

$$\psi_{i,j,l,m,n}^{(coag)} = \begin{cases} \dfrac{x_{n+1} - x_{i,j,l,m}'^{(coag)}}{x_{n+1} - x_n}; & if(x_n \le x_{i,j,l,m}'^{(coag)} < x_{n+1}) \\ \dfrac{x_{i,j,l,m}'^{(coag)} - x_{n-1}}{x_n - x_{n-1}}; & if(x_{n-1} \le x_{i,j,l,m}'^{(coag)} < x_n) \\ 0; & \text{otherwise} \end{cases} . \tag{16}$$

C. Theoretical parameter estimation

1. Binary homogenous nucleation

The binary nucleation theory proposed by Wyslouzil and Wilemski[19] is adopted in this study. Their theory starts from the following self-consistent expression for the concentration of the equilibrium binary cluster containing $n_{(A)}$ monomers of material A and $n_{(B)}$ monomers of material B, as

$$N_{eq}(n_{(A)}, n_{(B)}) = N_{S(A)}^{x_{(A)}} N_{S(B)}^{x_{(B)}} \exp(x_{(A)}\Theta_{(A)} + x_{(B)}\Theta_{(B)}) \times \exp\left[- \frac{W(n_{(A)}, n_{(B)})}{k_B T} \right], \tag{17}$$

$$x_{(A)} = \frac{n_{(A)}}{n_{(A)} + n_{(B)}} = 1 - x, \tag{18}$$

$$x_{(B)} = \frac{n_{(B)}}{n_{(A)} + n_{(B)}} = x, \tag{19}$$

and

$$\Theta_{(M)} = \frac{\sigma_{(M)} s_{mono(M)}}{k_B T}. \tag{20}$$

Therein, $N_{S(M)}$ signifies the monomer number density in equilibrium with pure liquid of material M, k_B represents Boltzmann's constant, T is the temperature, $\sigma_{(M)}$ denotes the surface tension of pure liquid of material M, and $s_{mono(M)}$ stands for the monomer's surface area of material M.

The free energy of formation of the cluster is given as

$$W(n_{(A)}, n_{(B)}) = - n_{(A)} k_B T \ln\left(\frac{N_{mono(A)}}{N_{S(A)}'} \right) - n_{(B)} k_B T \ln\left(\frac{N_{mono(B)}}{N_{S(B)}'} \right) + \sigma' s', \tag{21}$$

where $N_{mono(M)}$ is the monomer number density of material M and $N_{S(M)}'$ is the equilibrium monomer number density of material M in the saturated vapor over a bulk solution of composition x. In addition, σ' and s', respectively, denote the surface tension and the surface area of the cluster. Even though the surface tension is an important property determining the cluster formation, reliable data for binary clusters are not available at present. Furthermore, the approach from MDs or quantum dynamics is beyond the scope of this paper. Consequently, the following approximation is used:

$$\sigma' = x_{(A)}\sigma_{(A)} + x_{(B)}\sigma_{(B)}. \tag{22}$$

Although this simplified form might cause an error, this approximation is admissible for discussion at the present stage.

Most binary nucleation theories have indicated that binary clusters mainly grow up through the saddle point on the free energy surface W in $n_{(A)}-n_{(B)}$ space, except under the extreme conditions that Wyslouzil and Wilemski numerically tested using a hexanol–ethanol system.[19] For that reason, at the saddle point, a nucleus is definable as the cluster in the critical state. When the nucleus comprises $n_{(A)}^*$ monomers of

material A and $n^*_{(B)}$ monomers of material B, the nucleus' size v^* in Eq. (8) and composition x^* in Eq. (9) are written as

$$v^* = n^*_{(A)} v_{mono(A)} + n^*_{(B)} v_{mono(B)}, \tag{23}$$

and

$$x^* = \frac{n^*_{(B)}}{n^*_{(A)} + n^*_{(B)}}. \tag{24}$$

The quantities at the saddle point are denoted with superscript *.

Then, the homogeneous nucleation rate for a binary system is given as

$$I^* = I^*_{binary} = N_{eq}(n^*_{(A)}, n^*_{(B)}) R^* Z^* \left\{ \frac{\nu_+(\Delta l_+)}{2\Delta l_+} \mathrm{erf}\left[\Delta l_+ \left(\frac{w^*}{2k_B T} \right)^{1/2} \right] + \frac{\nu_-(\Delta l_-)}{2\Delta l_-} \mathrm{erf}\left[\Delta l_- \left(\frac{w^*}{2k_B T} \right)^{1/2} \right] \right\}. \tag{25}$$

This expression allows the direction of growth in the saddle region to be modified by the impingement rates of monomers and also assures a smooth transition between binary nucleation and unary nucleation.[19] The terms in Eq. (25) are described in Appendix B. It is noted that Eq. (25) cannot be used to estimate unary nucleation rates because it vanishes as either $N_{mono(A)}$ or $N_{mono(B)}$ approaches zero. Consequently, the following homogeneous nucleation rate for a unary system has additionally been derived in Ref. 19:

$$I^* = I^*_{unary(M)} = v_{mono(M)} N_{S(M)} N_{mono(M)} \left(\frac{2\sigma_{(M)}}{\pi m_{mono(M)}} \right)^{1/2} \left(1 + \frac{1}{n^{*1/3}_{(M)}} \right)^2 \left(1 + \frac{1}{n^*_{(M)}} \right)^{1/2} \exp\left[\Theta_{(M)} \left(1 - \frac{1}{3} n^{*2/3}_{(M)} \right) \right]. \tag{26}$$

2. Binary heterogeneous condensation

Once nuclei are generated by homogeneous nucleation, binary metal vapors condense on the nuclei heterogeneously, resulting in significant growth of the particles. The binary condensation is a key process to determine a nanopowder's profile. When the vapor of material M condenses on the particles at node (i,l), the volume increment $\Delta v_{(M)i,l}$ during the infinitesimal time increment Δt is estimated using the following equation with the rarefied gas effect correction.

$$\Delta v_{(M)i,l} = 2\pi d_i D_{mono(M)} v_{mono(M)} (N_{mono(M)} - \bar{N}_{S(M)i,l}) \times \left[\frac{0.75\alpha_{(M)}(1 + \mathrm{Kn}_i)}{0.75\alpha_{(M)} + 0.283\alpha_{(M)}\mathrm{Kn}_i + \mathrm{Kn}_i + \mathrm{Kn}_i^2} \right] \Delta t. \tag{27}$$

In that equation, d is the diameter, D_{mono} is the diffusion coefficient of the monomers estimated using Hirschfelder's formula,[22] and Kn is the Knudsen number which is defined as the ratio of the gas mean free path to the particle radius. The expression shown in Eq. (27) covers the entire range of Knudsen numbers.[23] In addition, α denotes the accommodation coefficient, which is known to be 0.013–0.38 for representative chemical materials on aqueous surfaces around room temperature.[23] However, the accommodation coefficients of Mo, Ti, and Si on their own silicides remain unknown at present. For that reason, they were all set to 0.1, i.e., $\alpha_{(\mathrm{Mo})} = \alpha_{(\mathrm{Ti})} = \alpha_{(\mathrm{Si})} = 0.1$ for this study.

This study presumes that each nanoparticle composing a nanopowder is a very small droplet of a binary mixture. The saturation pressure on such a nanoparticle' surface deviates from that on a flat surface of a pure liquid. Therefore, the saturated vapor concentration in Eq. (27) is given as a modified form as follows considering the effects of both mixture and surface curvature:[24]

$$\bar{N}_{S(M)i,l} = \Gamma_{(M)} x_{(M)l} N_{S(M)} \exp\left(\frac{4\sigma'_l v_{mono(M)}}{d_i k_B T} \right). \tag{28}$$

Therein, $\Gamma_{(M)}$ is the activity coefficient, which depends on interactions between two materials. In this study, the activity coefficients were set to unity because the exact values were not available for the target binary systems.

The composition (the content of material B) of the new particles which come from node (i,l) is calculated as

$$x'^{(cond)}_{i,l} = \left(n_{(B)i,l} + \frac{\Delta v_{(B)i,l}}{v_{mono(B)}} \right) \left(n_{(A)i,l} + \frac{\Delta v_{(A)i,l}}{v_{mono(A)}} + n_{(B)i,l} + \frac{\Delta v_{(B)i,l}}{v_{mono(B)}} \right)^{-1}, \tag{29}$$

where $n_{(M)i,l}$ denotes the number of M monomers in a single particle at node (i,l).

3. Coagulation of nanoparticles

Coagulation of nanoparticles plays a considerably important role in nanopowder growth. Although the collision frequency function $\beta_{i,j,l,m}$ in Eq. (14) is often described in the form for a free molecular regime, it is preferred that it can cover the wider range of particle sizes. Therefore, in this study, the Fuchs form of the collision frequency function is adopted[23] and modified for the present model. The collision frequency function between the particles at node (i,l) and the particles at node (j,m) is written as

$$\beta_{i,j,l,m} = 2\pi(D_i + D_j)(d_i + d_j) \left[\frac{d_i + d_j}{d_i + d_j + 2\sqrt{g^2_{i,l} + g^2_{j,m}}} + \frac{8(D_i + D_j)}{(d_i + d_j)\sqrt{\bar{c}^2_{i,l} + \bar{c}^2_{j,m}}} \right]^{-1}, \tag{30}$$

$$g_{i,l} = \frac{\pi \bar{c}_{i,l}}{24 D_i d_i} \left\{ \left(d_i + \frac{8D_i}{\pi \bar{c}_{i,l}} \right)^3 - \left[d_i^2 + \left(\frac{8D_i}{\pi \bar{c}_{i,l}} \right)^2 \right]^{3/2} \right\} - d_i, \tag{31}$$

and

$$\bar{c}_{i,l} = \left\{ \frac{8k_B T}{\pi v_i [\rho_{(A)}(1-x_l) + \rho_{(B)} x_l]} \right\}^{1/2}. \quad (32)$$

In those equations, $\rho_{(A)}$ and $\rho_{(B)}$, respectively, represent the densities of materials A and B. The diffusion coefficient D of each particle is given as follows by Refs. 23 and 25:

$$D_i = \frac{k_B T}{3\pi\mu d_i} \left\{ 1 + \mathrm{Kn}_i \left[A_1 + A_2 \exp\left(-\frac{2A_3}{\mathrm{Kn}_i} \right) \right] \right\}. \quad (33)$$

In that equation, $A_1=1.257$, $A_2=0.4$, and $A_3=0.55$; μ is the gas viscosity.

When a particle at node (i,l) and a particle at node (j,m) collide, merge, and consequently form a new larger particle, the new particle has composition (the content of material B) that is estimated as

$$x'^{(coag)}_{i,j,l,m} = \frac{n_{(B)i,l} + n_{(B)j,m}}{n_{(A)i,l} + n_{(A)j,m} + n_{(B)i,l} + n_{(B)j,m}}. \quad (34)$$

4. Vapor consumption

Nanoparticle growth is linked inextricably to vapor consumption because the concentration of material vapor determinately affects the features of homogeneous nucleation and heterogeneous condensation. Therefore, the population balance equations of the material monomers must be solved simultaneously.

$$\frac{dN_{mono(M)}}{dt} = [\dot{N}_{mono(M)}]_{nucl} + [\dot{N}_{mono(M)}]_{cond}. \quad (35)$$

In that equation, $[\dot{N}_{mono(M)}]$ represents the net production rate of the monomers of material M. The monomers are decreased by vapor consumption because of nucleation and condensation. The two terms of the right-hand side have negative values.

$$[\dot{N}_{mono(M)}]_{nucl} = -\sum_k I^* \xi_k^{(nucl)} n^*_{(M)}, \quad (36)$$

$$[\dot{N}_{mono(M)}]_{cond} = -\sum_i \sum_l \frac{N_{i,l} \Delta v_{(M)i,l}}{v_{mono(M)} \Delta t}. \quad (37)$$

Although Eq. (36) is described in a summation, only one term remains because the nucleation supplies particles to only the next larger nodes, as shown in Fig. 1(a).

5. Freezing point depression

During nanopowder growth with temperature decrease, the nanoparticles will be solidified. Once they are solidified, they can no longer increase their size as spherical particles by coagulation. They merely form their own aggregates. Indeed, several experimental reports describe that such aggregates were also generated in thermal plasma processing.[3,4,8] The present model addresses only spherical particles. Therefore, the computation of the coagulation growth must be stopped when the nanoparticles' temperature reaches their solidification points. Furthermore, the final profile of the nanopowder after solidification should be determined for evaluation which is usually done by comparison with experiment data. Nanopowders obtained from experiments are always in the solid state. Therefore, the freezing points of nanoparticles should be estimated correctly even though the nanoparticles have widely ranging sizes and compositions.

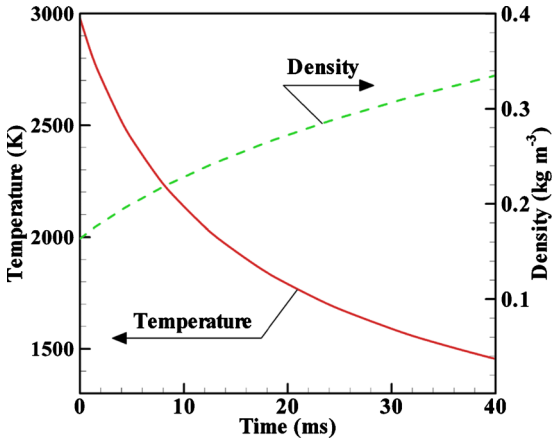

FIG. 2. (Color online) Cooling profiles of the bulk gas.

For inorganic materials, the freezing point T_{FP} of a particle decreases linearly with the particle diameter d, which is considerable especially for nanoparticles:[26]

$$T_{FP} = T_{FP,bulk} \left(1 - \frac{\varepsilon'}{d} \right), \quad (38)$$

and

$$\varepsilon' = x_{(A)} \varepsilon_{(A)} + x_{(B)} \varepsilon_{(B)}. \quad (39)$$

Parameter ε is a characteristic property determined by the solid and liquid surface energies and the bulk melting enthalpy. Furthermore, it should be considered that the freezing point in the bulk state $T_{FP,bulk}$ depends on the material composition (see Appendix C). According to the theoretical study by Wautelet *et al.*,[27] the solidus curves in the binary phase diagrams merely shift downward with the decrease in the particle diameter. Therefore, Eq. (38) is reasonably applicable to the evaluation of the freezing point depression of nanoparticles, even for binary systems.

III. COMPUTATIONAL CONDITIONS

The target process of this study is thermal plasma synthesis of nanopowders composed of binary alloy nanoparticles. Hence, the computation was conducted using a typical cooling condition at a plasma's tail where nanopowders are created, as depicted in Fig. 2. The bulk gas profiles of the temperature and the density were obtained numerically by the electromagnetic fluid dynamics approach for the identical conditions to the experiments which synthesized the metal–silicide nanopowders by an argon thermal plasma under atmospheric pressure.[8,9] The precursory coarse powders of a metal (Mo or Ti) and silicon were supplied as the raw materials at the total feed rate of 0.1 g min^{-1} with the silicon content of 66.7 at. %. Our previous numerical study confirmed that the raw materials were completely vaporized in the plasma operated at the flow rate of 34.0 Sl min^{-1}.[9] Because the vapors were transported with the gas flow to the plasma's tail, the material vapor concentrations correspond-

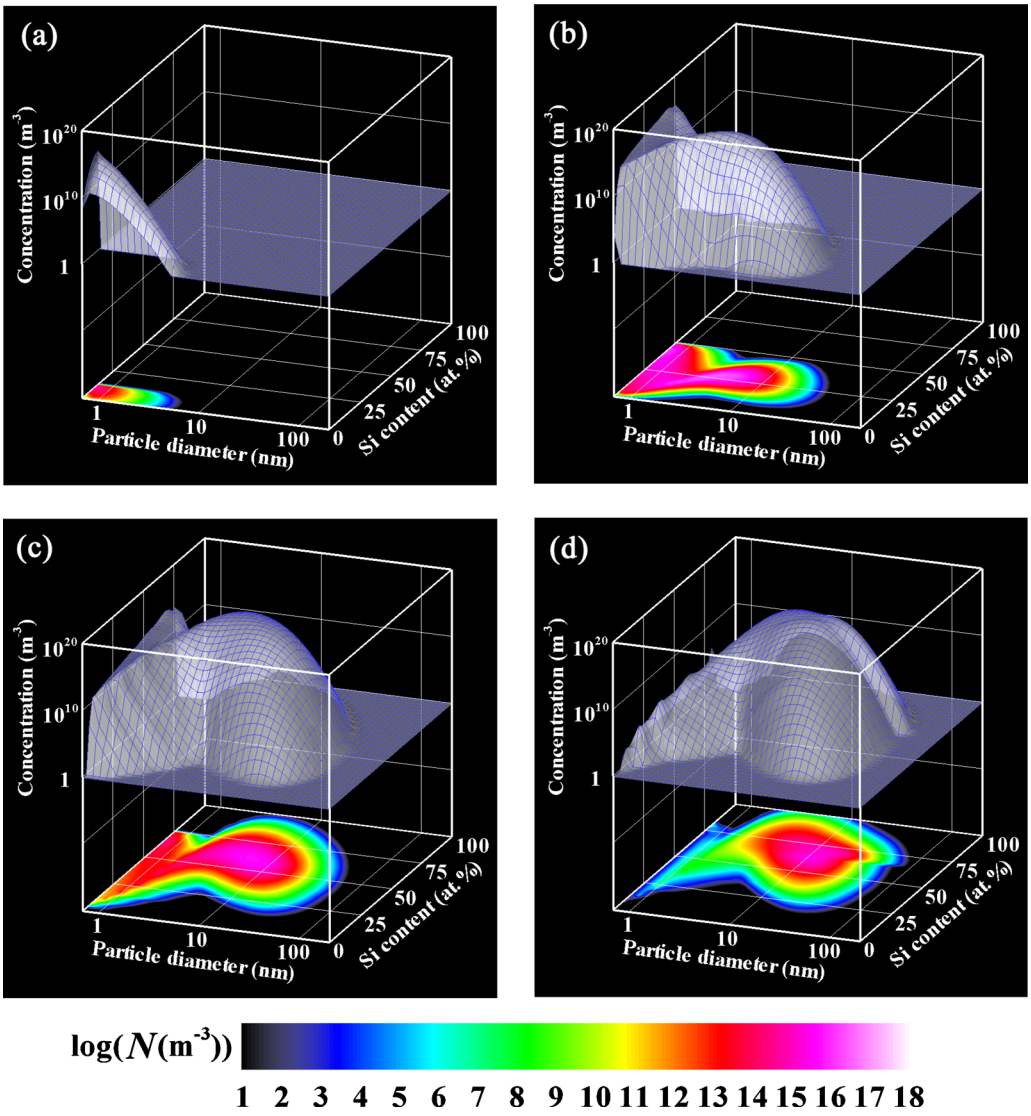

FIG. 3. (Color online) PSCDs of Mo–Si nanopowder at the growth time (a) τ=1.34 ms, (b) 5.91 ms, (c) 9.98 ms, and (d) 35.98 ms.

ing to those operating conditions were given as the initial condition. As implied in Fig. 2, the temperature-decrease rate also decreases from 1.5×10^5 to 1.0×10^4 K s^{-1} as time passes. Corresponding to that decrease in the rate, the computation was conducted with the time increment Δt increasing linearly from 5.0×10^{-6} to 2.0×10^{-5} s which provided sufficient resolution for the present target process as mentioned in Sec. II A. It is also noted that the population balance equations of the nanoparticles Eq. (6) and of the vapors Eq. (35) must be solved considering the increase in the bulk gas density. The material properties of the metals and silicon were obtained from the literature[28] (see Appendix D).

IV. RESULTS AND DISCUSSION

A. Binary growth of Mo–Si nanopowder

The Mo–Si binary vapors are cooled and consequently converted into nanoparticles. It is noteworthy that Mo vapor becomes supersaturated earlier than Si vapor because the saturation pressure of Mo is much smaller than that of Si (see Fig. 15 in Appendix D).

Figure 3 displays the evolution of the PSCD of the Mo–Si nanopowder, which is obtained using the present model. The conversion ratios of Mo and Si are also depicted in Fig. 4(a) to show how much of each material vapor has been converted into nanoparticles. In this study, the growth time τ was defined as the elapsed time after the nucleation started with the rate of 1.0×10^6 m^{-3} s^{-1} which is known as the critical nucleation rate. In the present Mo–Si system, the nucleation starts when the vapors of Mo and Si are cooled beneath 2940 K at t=0.26 ms. Thus, this value of time corresponds to τ=0 ms. Figure 3(a) shows that Mo-rich nuclei are generated at the early stage of the growth. Following nucleation, the nanoparticles are formed through cocondensation of the material vapors on the nuclei and coagulation among themselves. Figure 4(a) shows that the Mo vapor is converted earlier than Si vapor as noted above.

At τ=5.91 ms, 97% of Mo vapor has been converted into nanoparticles, although only 20% of Si vapor has been converted. In Fig. 3(b), the nanoparticles are still Mo-rich at this stage. Afterwards, because Si vapor condenses on those nanoparticles, their silicon contents as well as their diameters are increased [Fig. 3(c)]. At τ=9.98 ms, 99.9% of Mo vapor

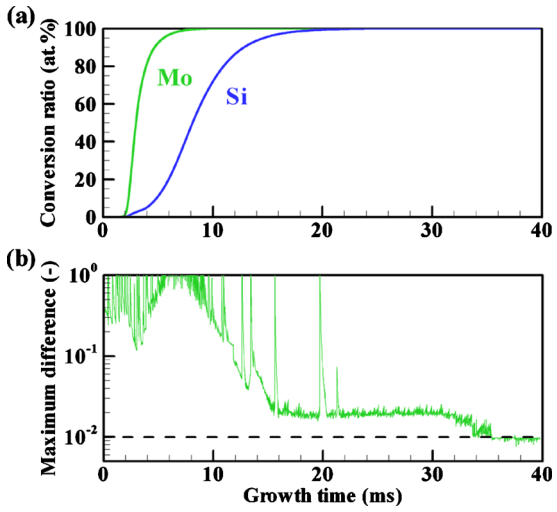

FIG. 4. (Color online) Characteristics of Mo–Si binary growth: (a) conversion ratio and (b) mature state determination. (The dashed line shows $Q=10^{-2}$.)

has already been converted. During those nanoparticles' growth, the binary nucleation is progressing simultaneously. For that reason, the nanopowder also has many nanoparticles or nuclei with $d<1$ nm and $x_{(Si)}=15-75$ at. % in its PSCD. It is noted that the nuclei are generated changing their size and composition because the material vapor pressures are also being changed by the vapor consumptions. Further discussion will be presented in the latter part of this section.

Figure 4(a) shows that the Mo–Si system has already consumed more than 99.9% of both Mo vapor and Si vapor by nucleation and condensation at $\tau=24.74$ ms. Because of the absence of the material vapors, the nanoparticles grow only through coagulation slowly. Finally, the nanoparticles form the mature state of the Mo–Si binary nanopowder at $\tau=35.98$ ms [Fig. 3(d)]. The mature nanopowder is composed mainly of the nanoparticles around $d=10$ nm and $x_{(Si)}=66.7$ at. %. The silicon content of 66.7 at. % was given as the initial condition, which intended the effective synthesis of $MoSi_2$ nanopowder because the silicon content of 66.7 at. % is the stoichiometric composition of $MoSi_2$. Therefore, the mature nanopowder mainly consists of the nanoparticles with the silicon content identical to the initially given silicon content. However, the nanopowder has the widely ranging compositions with the standard deviation of 5.37 at. %. The particle diameters also range widely even though the calculation was conducted under the simple condition.

To determine the mature state of a nanopowder, the maximum difference of the particle concentration at each node for Δt was monitored as shown in Fig. 4(b). That monitored parameter was defined as

$$Q = max\left(\frac{|\hat{N}_{i,j}^{(t)} - \hat{N}_{i,j}^{(t-\Delta t)}|}{\hat{N}_{i,j}^{(t-\Delta t)}}\right), \tag{40}$$

where

$$\hat{N}_{i,j}^{(t)} = \frac{N_{i,j}^{(t)}}{\rho_g^{(t)}}. \tag{41}$$

When Q fell to less than 10^{-2}, the nanopowder was determined to be mature. Therefore, the growth time at which the Mo–Si nanopowder became mature was $\tau=35.98$ ms. This idea is similar to the convergence judgment in computational fluid dynamics. Before computations were performed, we were concerned that the nanopowder might never reach its mature state—that small nanoparticles would continue to grow because their freezing points were lower [Fig. 14(a) in Appendix C] than the temperature given in the computational condition (Fig. 2). However, as Fig. 4(b) shows, even the maximum effect on the growth process is less than 1.0% in the whole nanopowder.

Figure 5 presents the evolution of the free energy surfaces W/k_BT for the Mo–Si binary nucleation. As described in Sec. II C 1, the clusters at the saddle point on the free energy surfaces are regarded as nuclei that can gain vapor molecules and thereby grow through condensation. Because W/k_BT varies with the change in the supersaturation ratio, the surface tension and the temperature according to Eq. (21), the size and composition of the nucleus also vary with the evolution of W/k_BT. The single nucleus comprises 14 Mo atoms and 2 Si atoms ($x_{(Si)}=12.5$ at. %) at $\tau=1.34$ ms, 7 Mo atoms and 2 Si atoms ($x_{(Si)}=22.2$ at. %) at $\tau=2.52$ ms, 6 Mo atoms and 6 Si atoms ($x_{(Si)}=50.0$ at. %) at $\tau=5.91$ ms, and 3 Mo atoms and 9 Si atoms ($x_{(Si)}=75.0$ at. %) at $\tau=9.98$ ms.

Figure 6 shows the compositions of the single nucleus and the nucleation rates at the representative growth times. During the earlier period, because of the much lower saturation pressure of Mo (see Fig. 15 in Appendix D), Mo vapor becomes supersaturated to a greater degree than Si vapor, the generated nuclei are Mo-rich. The Mo vapor is converted earlier than Si vapor; then the mixed material vapor becomes Si-rich, as shown in Fig. 4(a). As a consequence, the Mo-rich nuclei are generated in $\tau<5.91$ ms, whereas the Si-rich nuclei are generated in $\tau>5.91$ ms, as shown in Fig. 6.

Since our previous model[18] could simulate neither the binary nucleation nor the binary condensation, it predicted the following different growth behavior: pure Mo nanoparticles grew up following their own unary nucleation, and subsequently Si vapor condensed on the Mo nanoparticles. Such a growth behavior with a time lag of cocondensation implied that the nanoparticles possibly had Mo/Si core/shell structures. However, the actual experiment showed that the Mo–Si nanoparticles produced by a thermal plasma did not have any core/shell structures but had structures of intermetallic compounds.[9] On the other hand, the growth mechanism predicted by the present model indicates that the nanoparticles become intermetallic compounds by virtue of the consideration of binary nucleation and binary condensation.

B. Binary growth of Ti–Si nanopowder

Ti–Si system has a small difference of the saturation pressures, unlike Mo–Si system. Figures 7 and 8 present the binary growth behavior of the Ti–Si nanopowder. Ti–Si nu-

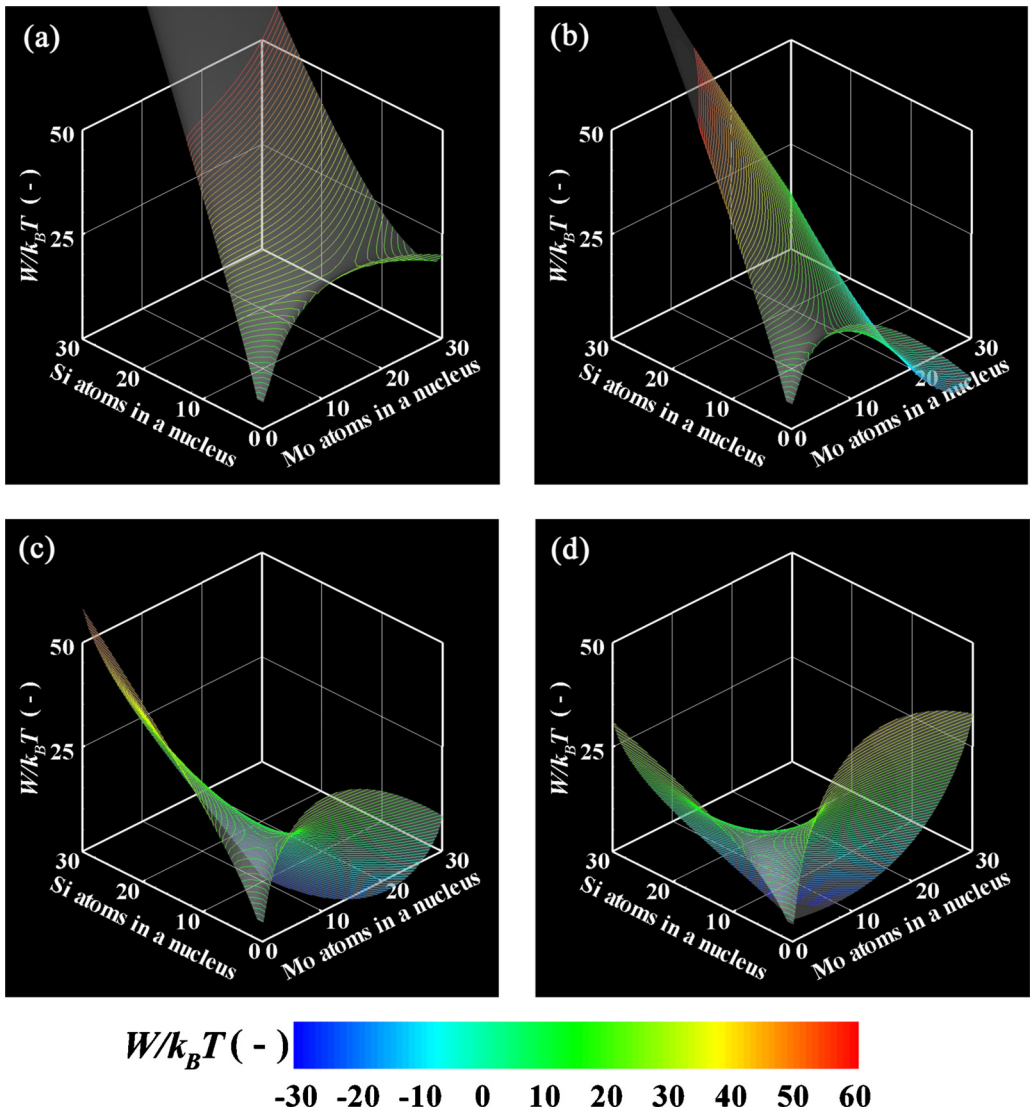

FIG. 5. (Color online) Free energy surfaces for Mo–Si binary nucleation at the growth time (a) τ=1.34 ms, (b) 2.52 ms, (c) 5.91 ms, and (d) 9.98 ms.

clei start to be generated when the material vapors are cooled beneath 2335 K at t=6.47 ms. This value of time corresponds to τ=0 ms in this Ti–Si system. Figure 8(a) shows that Ti vapor and Si vapor are decreased simultaneously by conversion, which is attributed to the nearly equal saturation pressures of Ti and Si. Following nucleation around τ =0.46 ms, Ti vapor and Si vapor are consumed dominantly by cocondensation. Then, 99.9% of Ti vapor finishes condensing at τ=13.25 ms, whereas 99.9% of Si vapor finishes condensing at τ=17.12 ms. After τ=17.12 ms, only coagulation contributes to the nanopowder's growth. According to Fig. 8(b), at τ=31.61 ms, the nanopowder reaches its mature state of Fig. 7(d). Compared with the Mo–Si nanopowder, the mature Ti–Si nanopowder has the narrower range of composition, with standard deviation of 1.96 at. %, which might indicate that simultaneous cocondensation results in a uniform composition in the mature binary alloy nanopowder. However, the particle diameters range widely from a few nanometers to 100 nm.

Figure 9 shows the evolution of the free energy surfaces W/k_BT for the Ti–Si binary nucleation. The saddle points on W/k_BT surface indicate that the single nucleus comprises 12 Ti atoms and 72 Si atoms ($x_{(Si)}$=85.7 at. %) at τ=0.46 ms, 2 Ti atoms and 24 Si atoms ($x_{(Si)}$=92.3 at. %) at τ =1.24 ms, 3 Ti atoms and 31 Si atoms ($x_{(Si)}$=91.2 at. %) at τ=2.06 ms, and 6 Ti atoms and 52 Si atoms ($x_{(Si)}$ =89.7 at. %) at τ=2.90 ms. The compositions of the single nucleus and the nucleation rates at the representative times are presented in Fig. 10. During the whole period of nucleation, the Ti–Si system produces Si-rich nuclei. Moreover, the nucleation period is much shorter than that in the Mo–Si system.

C. Model verification

To verify the present model, the numerical results are compared with a few available results of the experiments.[8,9] In the experiments, the synthesized nanopowders were collected at a sufficiently low-temperature region in the chamber where the nanopowders were presumed to have already completed their growth. The PSDs were measured from the micrographs obtained using transmission electron micros-

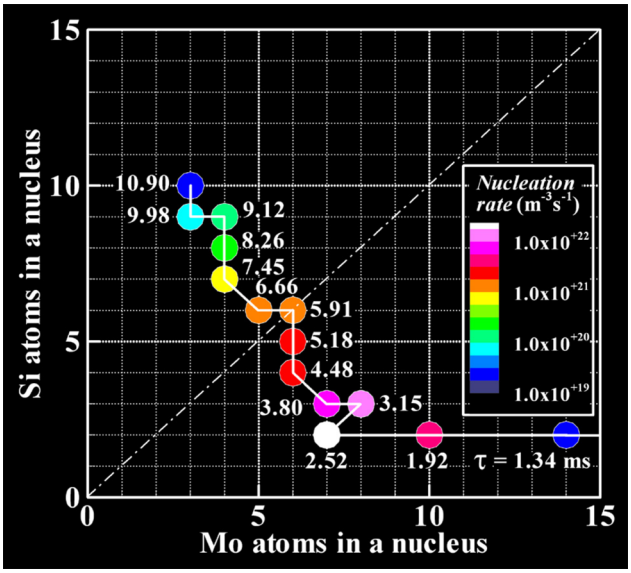

FIG. 6. (Color online) Evolutions of nucleus composition and nucleation rate in Mo–Si system. (The line segments merely show guidelines.)

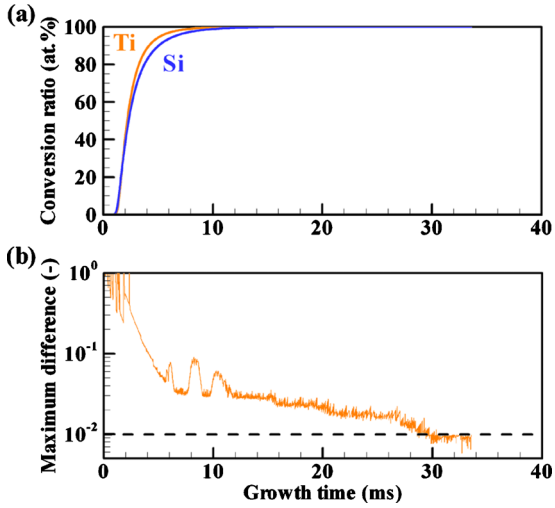

FIG. 8. (Color online) Characteristics of Ti–Si binary growth: (a) conversion ratio and (b) mature state determination. (The dashed line shows $Q = 10^{-2}$.)

copy (TEM) approximately for 1,000 nanoparticles. Observation by TEM (JEM-2010; JEOL) was conducted with accelerating voltage of 200 kV. The structures of the collected nanopowders were determined using x-ray diffractometry (MXP3TA; Mac Science Ltd.).

Figure 11 presents the PSD functions. Nanoparticles reside only at each node in the present model. Therefore, the size distribution based on the concentration should be converted into the PSD function. The size bin for the size node k was defined as

$$\Delta_k = \sqrt{v_{k+1}v_k} - \sqrt{v_k v_{k-1}}, \tag{42}$$

based on the logarithmic size space defined by Eq. (1). The PSD function was determined by presuming that this size bin includes all the nanoparticles at the size node k. The present numerical results and the experiment results show good agreements for the size distribution profiles as shown in Fig. 11. The arithmetic mean diameters of the Mo–Si nanopowder are estimated to be 10.6 nm in the present study and 13.1 nm in the experiment. Meanwhile, the Ti–Si nanopowders display almost the same arithmetic mean diameters of 16.9 nm in the present study and 16.7 nm in the experiment.

Our previous study[18] showed that the fractions of the silicides composing the nanopowder can be estimated quantitatively by comparing numerical data of the nanopowders' profiles with the binary phase diagrams.[29] Figure 12 presents a summary of the metal-silicide fractions which are predicted

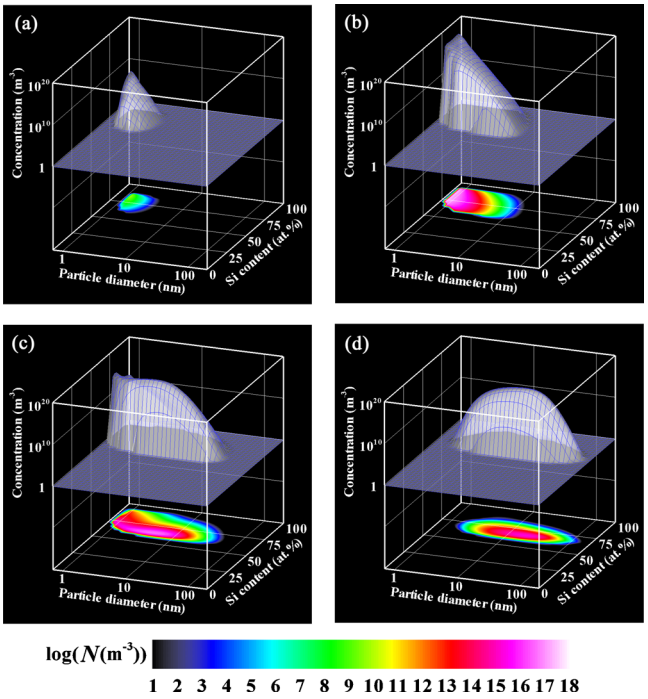

FIG. 7. (Color online) PSCDs of Ti–Si nanopowder at the growth time (a) τ=0.46 ms, (b) 1.24 ms, (c) 2.90 ms, and (d) 31.61 ms.

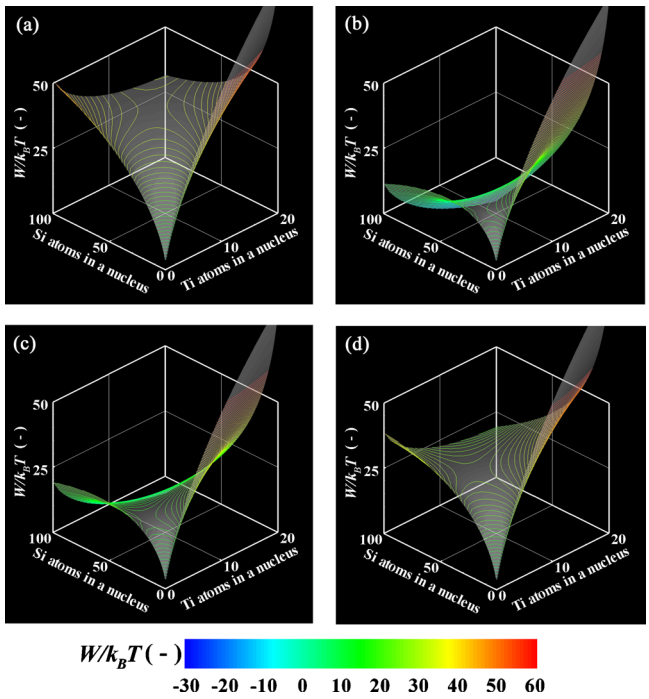

FIG. 9. (Color online) Free energy surfaces for Ti–Si binary nucleation at the growth time (a) τ=0.46 ms, (b) 1.24 ms, (c) 2.06 ms, and (d) 2.90 ms.

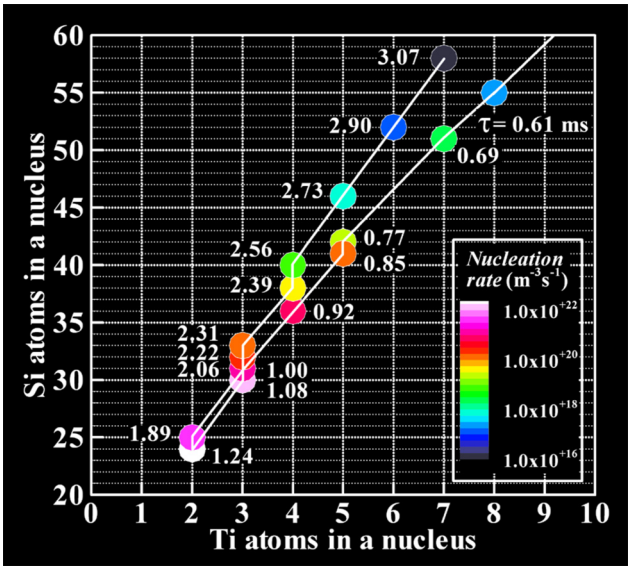

FIG. 10. (Color online) Evolutions of nucleus composition and nucleation rate in Ti–Si system. (The line segments merely show guidelines.)

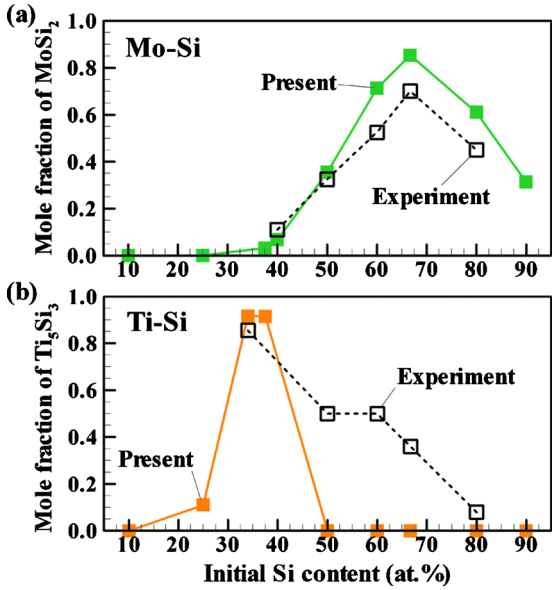

FIG. 12. (Color online) Effect of initial Si content on the metal–silicide fraction in (a) Mo–Si nanopowder and (b) Ti–Si nanopowder. (Experiment results were obtained from Ref. 8.)

using the present numerical results for several silicon contents given as the initial conditions. The present results and the experiment data show almost the same tendencies for $MoSi_2$ nanopowders. Figure 12(a) also shows that the largest number of $MoSi_2$ nanoparticles are synthesized with the initial silicon content of 66.7 at. %. For the Ti–Si nanopowders, Fig. 12(b) shows that the initial silicon contents of 34.0 and 37.5 at. % result in the most effective synthesis of Ti_5Si_3 nanoparticles. However, when the initial silicon content is set to be smaller than 34.0 at. % or larger than 37.5 at. %, the fraction of Ti_5Si_3 becomes drastically smaller. These results suggest that the initial silicon content in the raw materials should be set to the stoichiometric composition to synthesize as many nanoparticles of the desired compound as possible. In this way, the present model can

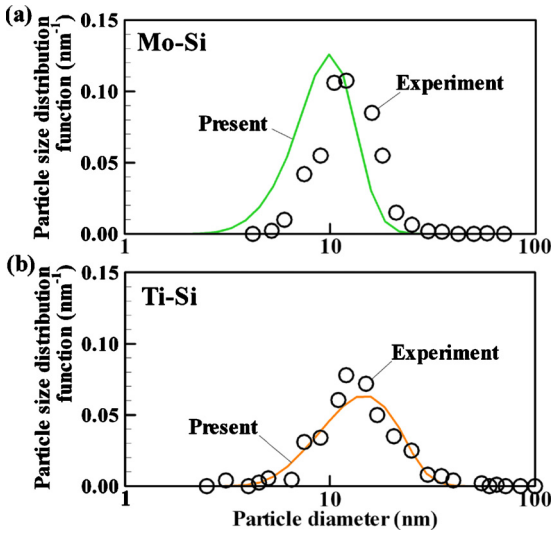

FIG. 11. (Color online) PSD functions of the mature nanopowders in (a) Mo–Si system and (b) Ti–Si system. [Experiment results were obtained from Ref. 9 for (a) and Ref. 8 for (b).]

also be used for compound prediction. However, it is noted that the use of equilibrium phase diagrams for postprocessing causes an oversimplified estimation of compounds because thermal plasma synthesis of nanopowders progresses under a nonequilibrium condition with a rapid temperature decrease. Nevertheless, the present model helps us predict the synthesized compounds somewhat.

As described above, the numerical results and the experiment results agree well mutually from the viewpoint of the particle size as well as the composition. However, those agreements are qualitative even though they appear quantitative, because the present computation was not the complete reproduction of the experiment. Further discussions are described as follows.

First of all, it should be noted that experiments of practical material processing by thermal plasmas inherently include errors because thermal plasmas are often accompanied with unstably unsteady thermofluid fields. Indeed, it is often reported that some unvaporized raw-material particles with large diameters are detected, even though numerical calculation predicts complete vaporization of the raw materials.

On the other hand, the present numerical results also include errors because the present model has been constructed with some simplifications. The present model cannot calculate the coagulation between a solid particle and a liquid particle. When a solid particle and a liquid particle collide, they could form a nonspherical agglomerate, which the present model cannot express. Sintering effects might also be considerable on coagulation. Meanwhile, the splitting scheme for the nodal approximation does not keep a PSD monodisperse in the condensational growth.[21] However, as reported by many experimental studies and even the numerical studies which calculated the condensational growth without the splitting scheme,[14,15] nanopowders synthesized by

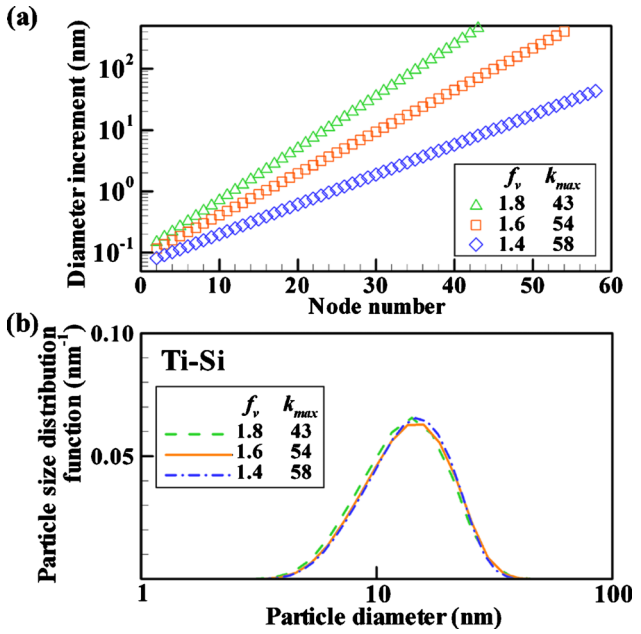

FIG. 13. (Color online) Effect of size spacing and number of nodes: (a) diameter increments and (b) PSD functions of mature Ti–Si nanopowders.

thermal plasmas almost always become polydisperse through their growth. Hence, the infeasibility to keep a PSD monodisperse does not cause a crucial error.

In addition, the present model incorporates neither condensational heat generation nor the electric charge of nanoparticles. The heat generation can possibly increase the temperatures of the nanoparticles and the bulk gas, which will affect the growth process of the nanoparticles. The electric charge of nanoparticles would also affect the nanoparticles' collisions. Furthermore, the present model required the adoption of data related to the surface tensions of the bulk materials to calculate the formation of nuclei, even though those data are not strictly accurate for nuclei with very small diameters of subnanometers. However, the appropriate data for binary clusters are not available. Consequently, we selected an acceptable mode of calculating the surface tensions of a binary nucleus Eq. (22) using the data of the bulk materials. The present model also regards a nucleus as a small spherical particle, although it was reported that the nucleus shape affects the nucleation barrier.[30] The shape effect should also be considered for calculation that is more accurate.

Although such issues remain to be improved, we can conclude that the present model effectively simulates the whole growth process of nanopowders through binary homogeneous nucleation, binary heterogeneous cocondensation, and coagulation among binary alloy nanoparticles. Additionally, using other materials' properties, nanopowder growths for binary alloys with other combinations can also be simulated.

It is noted that the computation was performed to investigate how the present model simulated nanopowders' growth behaviors with time evolution as the first stage of study. However, actual nanopowder growths take place in a three-dimensional space. Nanopowders that grow in different regions will have different profiles. Because of Brownian motion and thermophoresis, those nanopowders diffuse, merge and create new different profiles. Considering that effect, the present model is expected to be implemented in three-dimensional simulations in the future.

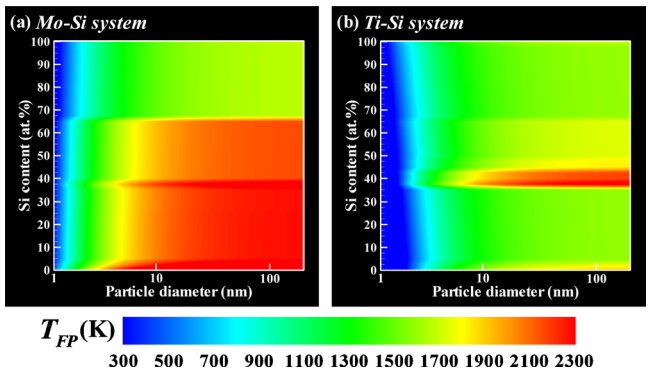

FIG. 14. (Color online) Freezing point charts for binary systems: (a) Mo–Si system and (b) Ti–Si system.

V. SUMMARY

A unique model was developed for numerical analysis of the entire growth process of binary alloy nanopowders in thermal plasma synthesis. The effect of the freezing point depression due to nanoscale particle diameters was also considered. The model can express any nanopowder profile in the PSCD. Moreover, its numerical solution algorithm is arithmetic and straightforward so that the model is easy to use. By virtue of these features, the model effectively simulated the collective and simultaneous combined process of binary homogeneous nucleation, binary heterogeneous cocondensation, and coagulation among nanoparticles.

In this study, the metal–silicon systems were particularly chosen as representative binary systems involving cocondensation processes. In consequence, the numerical calculation with the present model revealed the growth mechanisms of the Mo–Si and Ti–Si nanopowders by exhibiting their PSCD evolutions. The difference of the materials' saturation pressures strongly affects the growth behaviors and mature states of the binary alloy nanopowder.

ACKNOWLEDGMENTS

This work was supported by Japan Society for the Promotion of Science Grant-in-Aid for Young Scientists (B) (Grant No. 20760106). The authors gratefully acknowledge Dr. Y. Nagao of Tohoku University for meaningful discussion.

APPENDIX A

Figure 13 presents the effect of size spacing and number of nodes on the numerical results. We tested several calculations with the different spacing factors for size f_v and number of nodes k_{max}. Even though the diameter increments in

TABLE I. Material properties.

Material	Atomic diameter (nm)	Surface tension (N m^{-1})
Mo	0.272	2.250–0.000 30 (T–2880)
Ti	0.294	1.650–0.000 26 (T–1958)
Si	0.234	0.865–0.000 13 (T–1683)

the three cases have large differences ranging from a few times to a few hundred times, almost the same numerical results are obtained. This fact means that the present model does not have a dependency on the size resolution with the values around $f_v=1.6$ and $k_{max}=54$. Therefore, those value were chosen in this study.

APPENDIX B

In the binary nucleation theory proposed by Wyslouzil and Wilemski,[19] the homogeneous nucleation rate for a binary system is given as

$$I^* = I^*_{binary} = R^* Z^* N_{eq}(n^*_{(A)}, n^*_{(B)}) \times \left\{ \frac{\nu_+(\Delta l_+)}{2\Delta l_+} \mathrm{erf}\left[\Delta l_+ \left(\frac{w^*}{2k_B T} \right)^{1/2} \right] + \frac{\nu_-(\Delta l_-)}{2\Delta l_-} \mathrm{erf}\left[\Delta l_- \left(\frac{w^*}{2k_B T} \right)^{1/2} \right] \right\}. \quad \text{(B1)}$$

This expression allows the direction of growth in the saddle region to be modified by

$$R^* = \frac{\gamma^*_{f(A)} \gamma^*_{f(B)} N_{mono(A)} N_{mono(B)}}{\gamma^*_{f(A)} N_{mono(A)} \sin^2 \phi + \gamma^*_{f(B)} N_{mono(B)} \cos^2 \phi}, \quad \text{(B2)}$$

and

$$Z^* = -\frac{W^*_{AA} \cos^2 \phi + 2W^*_{AB} \cos \phi \sin \phi + W^*_{BB} \sin^2 \phi}{(W^{*2}_{AB} - W^*_{AA} W^*_{BB})^{1/2}}. \quad \text{(B3)}$$

The angle ϕ is determined by

$$\phi = \tan^{-1}\left\{ \frac{W^*_{BB} - \chi^* W^*_{AA}}{2\chi^* W^*_{AB}} + \left[\left(\frac{W^*_{BB} - \chi^* W^*_{AA}}{2\chi^* W^*_{AB}} \right)^2 + \frac{1}{\chi^*} \right]^{1/2} \right\}, \quad \text{(B4)}$$

with

$$\chi^* = \frac{\gamma^*_{f(A)} N_{mono(A)}}{\gamma^*_{f(B)} N_{mono(B)}}. \quad \text{(B5)}$$

The forward rate coefficient of nucleus formation is written as

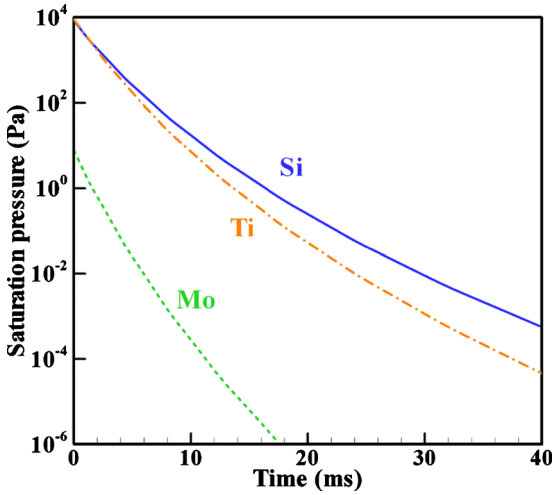

FIG. 15. (Color online) Saturation pressure curves of the materials corresponding to the present computational condition.

$$\gamma^*_{f(M)} = \pi (d_{mono(M)} + d^*)^2 \left[\frac{k_B T (m_{mono(M)} + m^*)}{2\pi m_{mono(M)} m^*} \right]^{1/2}, \quad \text{(B6)}$$

where m denotes the mass. W_{AA}, W_{AB}, and W_{BB} are the second derivatives of W.

Equation (B1) also assures a smooth transition between binary and unary nucleation by the prefactor. The terms in the prefactor are given as

$$w^* = -\frac{W^*_{AA} W^*_{BB} - W^{*2}_{AB}}{W^*_{AA} \cos^2 \phi + 2W^*_{AB} \cos \phi \sin \phi + W^*_{BB} \sin^2 \phi}, \quad \text{(B7)}$$

$$\Delta l_+ = \frac{n^*_{(B)}}{\cos \phi}, \quad \text{(B8)}$$

$$\Delta l_- = \frac{n^*_{(A)}}{\sin \phi}, \quad \text{(B9)}$$

and

$$\Delta \nu_\pm (\Delta l_\pm) = max(1, \Delta l_\pm). \quad \text{(B10)}$$

The detailed discussion is found in Ref. 19.

APPENDIX C

The freezing points of the bulk materials for the metal–silicon systems were obtained from the binary phase diagrams.[29] The solidus curves in the diagrams were approximated linearly. The following values were used in Eq. (38).

$$T_{FP,bulk}(\mathrm{Mo-Si}) = \begin{cases} 2896 - 14950x_{(\mathrm{Si})}; & if(0.000 \le x_{(\mathrm{Si})} < 0.040) \\ 2298; & if(0.040 \le x_{(\mathrm{Si})} < 0.257) \\ 2293; & if(0.257 \le x_{(\mathrm{Si})} < 0.370) \\ 2293 + 32000(x_{(\mathrm{Si})} - 0.370); & if(0.370 \le x_{(\mathrm{Si})} < 0.375) \\ 2453 - 11200(x_{(\mathrm{Si})} - 0.375); & if(0.375 \le x_{(\mathrm{Si})} < 0.400) \\ 2173; & if(0.400 \le x_{(\mathrm{Si})} < 0.667) \\ 1673; & if(0.667 \le x_{(\mathrm{Si})} < 1.000) \\ 1687; & if(x_{(\mathrm{Si})} = 1.000) \end{cases},$$

$$T_{FP,bulk}(\mathrm{Ti-Si}) = \begin{cases} 1943 - 7234x_{(\mathrm{Si})}; & if(0.000 \le x_{(\mathrm{Si})} < 0.047) \\ 1603; & if(0.047 \le x_{(\mathrm{Si})} < 0.355) \\ 1603 + 799.98(x_{(\mathrm{Si})} - 0.355); & if(0.355 \le x_{(\mathrm{Si})} < 0.375) \\ 2403 - 10500(x_{(\mathrm{Si})} - 0.375); & if(0.375 \le x_{(\mathrm{Si})} < 0.395) \\ 2193; & if(0.395 \le x_{(\mathrm{Si})} < 0.444) \\ 1843; & if(0.444 \le x_{(\mathrm{Si})} < 0.500) \\ 1583; & if(0.500 \le x_{(\mathrm{Si})} < 0.667) \\ 1532; & if(0.667 \le x_{(\mathrm{Si})} < 1.000) \\ 1687; & if(x_{(\mathrm{Si})} = 1.000) \end{cases}.$$

In this study, the values calculated by Guisbiers *et al.*[26] for a spherical particle were adopted: $\varepsilon_{(\mathrm{Mo})}=1.06$ nm, $\varepsilon_{(\mathrm{Ti})}=1.78$ nm, and $\varepsilon_{(\mathrm{Si})}=1.16$ nm.

Figure 14 presents the freezing point charts of nanoparticles for Mo–Si and Ti–Si systems. The smaller nanoparticles have lower freezing points. The computation of the coagulation growth of nanoparticles at each node was stopped when their temperature decreased and reached each freezing point.

The data of the freezing points are interpolated in the present model. However, the values for nanoparticles smaller than 6 nm are not strictly accurate because Eq. (38) was derived based on thermodynamics.[27] To obtain values that are more accurate for such smaller nanoparticles, other approaches should be required, which unfortunately deviates from the theme of this paper.

APPENDIX D

The temperature-dependence data of the materials were obtained from Ref. 28. The specific data of the atomic diameters and the temperature-dependent surface tensions are summarized in Table I. The saturation pressure curves corresponding to the present computation condition are drawn in Fig. 15. Because the temperature of the bulk gas decreases as time passes, the saturation pressures of the materials also decrease. Mo–Si binary system has a large saturation pressure difference between the two materials. On the other hand, Ti–Si binary system has a small difference of the saturation pressures.

[1]R. W. Siegel, Mater. Sci. Eng., A **168**, 189 (1993).
[2]K. Matsuura, T. Hasegawa, T. Ohmi, and M. Kudoh, Metall. Mater. Trans. A **31**, 747 (2000).
[3]X. Fan and T. Ishigaki, J. Cryst. Growth **171**, 166 (1997).
[4]X. Fan, T. Ishigaki, and Y. Sato, J. Mater. Res. **12**, 1315 (1997).
[5]J. H. J. Scott, K. Chowdary, Z. Turgut, S. A. Majetich, and M. E. McHenry, J. Appl. Phys. **85**, 4409 (1999).
[6]T. Watanabe, H. Itoh, and Y. Ishii, Thin Solid Films **390**, 44 (2001).
[7]S. Son, M. Taheri, E. Carpenter, V. G. Harris, and M. E. McHenry, J. Appl. Phys. **91**, 7589 (2002).
[8]T. Watanabe and H. Okumiya, Sci. Technol. Adv. Mater. **5**, 639 (2004).
[9]M. Shigeta and T. Watanabe, J. Phys. D: Appl. Phys. **40**, 2407 (2007).
[10]T. Sato, M. Shigeta, D. Kato, and H. Nishiyama, Int. J. Therm. Sci. **40**, 273 (2001).
[11]M. Shigeta, T. Sato, and H. Nishiyama, Int. J. Heat Mass Transfer **47**, 707 (2004).
[12]M. Shigeta and H. Nishiyama, ASME Trans. J. Heat Transfer **127**, 1222 (2005).
[13]N. Lümmen and T. Kraska, Eur. Phys. J. D **41**, 247 (2007).
[14]M. Shigeta and T. Watanabe, J. Mater. Res. **20**, 2801 (2005).
[15]M. Shigeta and T. Watanabe, Thin Solid Films **515**, 4217 (2007).
[16]A. Vorobev, O. Zikanov, and P. Mohanty, J. Phys. D: Appl. Phys. **41**, 085302 (2008).
[17]A. Vorobev, O. Zikanov, and P. Mohanty, J. Therm. Spray Technol. **17**, 956 (2008).
[18]M. Shigeta and T. Watanabe, J. Therm. Spray Technol. **18**, 1022 (2009).
[19]B. E. Wyslouzil and G. Wilemski, J. Chem. Phys. **103**, 1137 (1995).
[20]S. K. Friedlander, *Smoke, Dust and Haze, Fundamentals of Aerosol Dynamics*, 2nd ed. (Oxford University Press, New York, 2000).
[21]A. Prakash, A. P. Bapat, and M. R. Zachariah, Aerosol Sci. Technol. **37**, 892 (2003).
[22]J. O. Hirschfelder, C. F. Curtiss, and R. B. Bird, *Molecular Theory of Gases and Liquids* (Wiley, New York, 1964).
[23]J. H. Seinfeld and S. N. Pandis, *Atmospheric Chemistry and Physics, From Air Pollution to Climate Change* (Wiley, New York, 1998).
[24]T. Vesala, M. Kulmala, R. Rudolf, A. Vrtala, and P. E. Wagner, J. Aerosol Sci. **28**, 565 (1997).
[25]G. M. Phanse and S. E. Pratsinis, Aerosol Sci. Technol. **11**, 100 (1989).

[26]G. Guisbiers, M. Kazan, O. V. Overschelde, M. Wautelet, and S. Pereira, J. Phys. Chem. C **112**, 4097 (2008).
[27]M. Wautelet, J. P. Dauchot, and M. Hecq, Nanotechnology **11**, 6 (2000).
[28]Japan Institute of Metals, *Metal Data Book* (Maruzen, Tokyo, 1993).
[29]T. B. Massalski, *Binary Alloy Phase Diagrams*, 2nd ed. (American Society for Metals, Materials Park, Ohio, 1990), Vol. 3.
[30]R. Swaminathan, M. A. Willard, and M. E. McHenry, Acta Mater. **54**, 807 (2006).